 MCB, vol.9, no.1, pp.31-53, 2012

Transient Bioheat Simulation of the Laser-Tissue Interaction in Human Skin Using Hybrid Finite Element Formulation

Ze-Wei Zhang[*], Hui Wang[†] and Qing-Hua Qin[*,‡]

Abstract: This paper presents a hybrid finite element model for describing quantitatively the thermal responses of skin tissue under laser irradiation. The model is based on the boundary integral-based finite element method and the Pennes bioheat transfer equation. In this study, temporal discretization of the bioheat system is first performed and leads to the well-known modified Helmholtz equation. A radial basis function approach and the boundary integral based finite element method are employed to obtain particular and homogeneous solutions of the laser-tissue interaction problem. In the boundary integral based finite element formulation, two independent fields are assumed: intra-element field and frame field. The intra-element field is approximated through a linear combination of fundamental solutions at a number of source points outside the element domain. The frame temperature field is expressed in terms of nodal temperature and the corresponding shape function. Numerical examples are considered to verify and assess the proposed numerical model. Sensitivity analysis is performed to explore the thermal effects of various control parameters on tissue temperature and to identify the degree of burn injury due to laser heating.

Keywords: Bioheat transfer; laser irradiation; burn; hybrid finite element; fundamental solution; radial basis function

Symbols

c	Specific heat of tissue ($\mathrm{Jkg^{-1}K^{-1}}$)
c_b	Specific heat of blood ($\mathrm{Jkg^{-1}K^{-1}}$)
h_∞	Convection coefficient of ambient fluid ($\mathrm{Wm^{-2}K^{-1}}$)

[*] Research School of Engineering, Australian National University, Canberra, ACT 0200, Australia
[†] Institute of Scientific and Engineering Computation, Henan University of Technology, Zhengzhou 450001, PR China
[‡] Corresponding author, qinghua.qin@anu.edu.au

k	Thermal conductivity of tissue ($\mathrm{Wm^{-1}K^{-1}}$)
L	Width of 2D skin model (m)
P_{in}	Laser power setting (W)
q	Heat flux ($\mathrm{Wm^{-2}}$)
Q_m	Metabolic heat of tissue ($\mathrm{Wm^{-3}}$)
Q_r	Spatial heat ($\mathrm{Wm^{-3}}$)
Q_t	Sum of metabolic heat and spatial heat ($\mathrm{Wm^{-3}}$)
t	Time (s)
Δt	Time step (s)
T	Temperature of tissue (^{o}C)
T_a	Artery temperature (^{o}C)
T_c	Temperature of body core (^{o}C)
T_∞	Sink temperature of ambient fluid (^{o}C)
ρ	Density of tissue ($\mathrm{kgm^{-3}}$)
ρ_b	Density of blood ($\mathrm{kgm^{-3}}$)
σ	Standard deviation of laser beam profile (m)
ω_b	Blood perfusion rate ($\mathrm{m^3s^{-1}m^{-3}}$)
μ_a	Absorption coefficient of tissue ($\mathrm{m^{-1}}$)
P	Pre-exponential factor ($\mathrm{s^{-1}}$)
ΔE	Activation energy ($\mathrm{Jkmol^{-1}}$)
R	Universal gas constant ($\mathrm{Jkmol^{-1}K^{-1}}$)

1 Introduction

In diagnostic applications to biological systems, varieties of laser therapy are widely used to cure pathology ranging from tumor to short sight; however, the laser heating can cause burning injury due to local high temperature. It is therefore important to accurately predict the temperature distribution induced and the potential burn damage to healthy human tissue during laser irradiation. This can be achieved by effective prediction of bioheat transport [1]. It is noted that cost and other factors preclude real time measurement of temperature distribution in in vivo tissue. Thus numerical simulation of bioheat transfer may be attractive and necessary in practice. Marqa et al. investigated bioheat and thermal damage behavior under laser irradiation using the conventional finite element method (FEM) [2], which was also used by Shibib to determine the thermal damage in human skin due to laser irradiation [3]. Ansari et al. studied short-pulse laser propagation in biological tissue by means of the boundary element method (BEM) with time-dependent fundamental solutions [4]. The Monte Carlo method and the dual reciprocity boundary element method (DRBEM) have also been applied to evaluate transient or steady

state thermal behaviors in biological tissues [5-7]. Recently, a method of fundamental solutions (MFS) was developed and applied to the problem of heat transfer in skin tissue [8].

Among the existing computational methods, Green's functions or fundamental solution based methods such as the BEM/DRBEM and the MFS have been successfully developed to obtain highly accurate numerical approximations of solutions to linear elliptic partial differential equations (PDEs). The use of fundamental solutions makes the boundary element or collocation discretization possible in these methods to preserve their boundary-only merits. As an alternative to BEM and MFS, a fundamental solutions based hybrid finite element model, HFS-FEM for short, was presented in [9], retaining the advantages of both boundary integrals in BEM and flexible element division in FEM, and it has been applied to the problem of heat transfer in the human eye [10], fiber-composites [11] and plane elasticity [12, 13]. In the proposed HFS-FEM formulation, the solution inside an element is approximated by a linear combination of fundamental solutions with sources located outside the element, as in the MFS [14], and the conventional shape function interpolation is used to approximate the independent frame field defined over the element boundary. The linkage of the two groups of independent fields is established through use of a hybrid variational functional (presented in Section 3.3).

In this study, a HFS-FEM model coupled with the dual reciprocity technique is developed for analyzing transient bioheat transfer in laser treatment. First, a backward time stepping scheme is employed to perform the time discretization, leading to the inhomogeneous modified Helmholtz system. Then, the particular solution part of the inhomogeneous system is obtained using the interpolation of radial basis functions (RBFs) at a number of points in the solution domain. The homogeneous solution part is obtained using the hybrid finite element model. Finally, numerical results are presented to verify and assess the numerical approach and to illustrate the effect of laser power on temperature distribution in skin tissue.

The paper is organized as follows: In Section 1, a general transient bioheat model of two-dimensional skin tissue is described, providing notations and reference for the subsequent sections. The solution procedures for the HFS-FEM combined with RBF are presented in Sections 2 and 3. In Section 4, validation of the proposed algorithm, sensitivity analysis of the control parameters, and burn prediction are conducted. Finally some conclusions are presented in Section 5.

2 Bioheat mathematical model in skin tissue

2.1 Skin tissue under laser heating

The two-dimensional skin model used in [5] is chosen here, in which the skin material is assumed to be homogeneous and isotropic. In the model displayed in Figure 1, the outer surface of the skin tissue is subjected to the convention condition and the inner boundary is distant from the skin surface, where the temperature remains at the constant core temperature. The upper and lower surfaces are treated as adiabatic by assuming that tissue remote from the area of interest is not affected by the imposed thermal disturbance. A Gaussian type laser beam is introduced as the internal spatial heat source and the Beer-Lambert law is used to model the exponential decay of heat generation by laser heating inside the tissue.

Due to the symmetry of the skin model, only half of the model is taken into consideration in the analysis, say the upper half shaded region displayed in Figure 1, in which x denotes the tissue depth from the skin surface, y is the distance along the skin surface, and a rectangular domain of 4cm length and 3cm width is employed as the solution domain [5]. The thermal properties of skin tissues used in the analysis are listed in Table 1 [8].

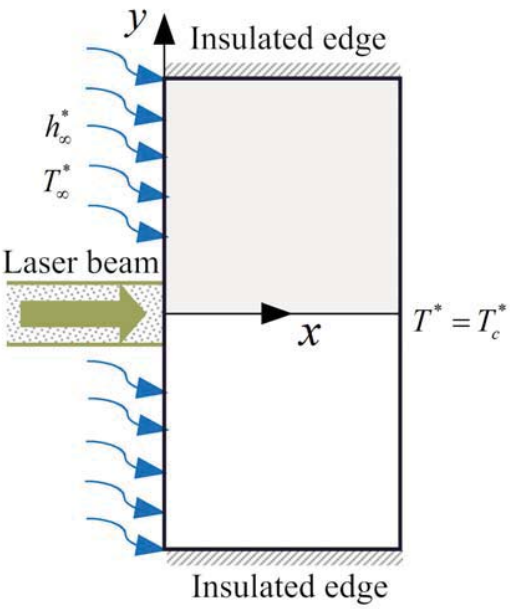

Figure 1: Simplified skin model of two-dimensional skin tissue

As shown in Figure 1, the laser beam, assumed to be produced from a CO_2 laser with scanner head and beam expander, injects directly onto the middle point (0, 0) of the skin surface. In the present work, the pattern of the laser beam is that of

Table 1: Thermal properties of skin tissue

Thermal properties of skin	*Value*
Thermal conductivity k ($\mathrm{Wm^{-1}K^{-1}}$)	0.5
Density ρ ($\mathrm{kgm^{-3}}$)	1000
Specific heat c ($\mathrm{Jkg^{-1}K^{-1}}$)	4200
Blood perfusion rate ω_b ($\mathrm{m^3s^{-1}m^{-3}}$)	0.0005
Density of blood ρ_b ($\mathrm{kgm^{-3}}$)	1000
Specific heat of blood c_b ($\mathrm{Jkg^{-1}K^{-1}}$)	4200
Metabolic heat Q_m ($\mathrm{Wm^{-3}}$)	4200

Gaussian distribution with 2.85mm standard deviation [15]. The Beer-Lambert law is used to model the laser heat absorption in the two dimensional skin model, and thus the spatial heat source Q_r caused by laser heating is described by

$$Q_r^*(x,y,t) = P_{in}\mu_a e^{(-\mu_a x)} \frac{1}{\sigma\sqrt{2\pi}} e^{\left(\frac{-y^2}{2\sigma^2}\right)} \tag{1}$$

where P_{in} represents the laser power setting, μ_a the absorption coefficient of the skin tissue determined by the wave length of the laser, and σ is the standard deviation of the laser beam profile.

2.2 General mathematical equations

Referring to the Cartesian coordinate system shown in Figure 1, the bioheat transfer in a biological tissue is adequately described by the well-known Pennes equation in the following general form:

$$k^*\nabla^2 T^* + \rho_b^* c_b^* \omega_b^* (T_a^* - T^*) + Q_t^* = \rho^* c^* \frac{\partial T^*}{\partial t^*} \qquad \mathbf{x} \in \Omega \tag{2}$$

with the boundary conditions

$$\begin{cases} T^*(\mathbf{x},t^*) = \bar{T}^*(\mathbf{x},t^*) & \mathbf{x} \in \Gamma_1 \\ q^*(\mathbf{x},t^*) = \bar{q}^*(\mathbf{x},t^*) & \mathbf{x} \in \Gamma_2 \\ q^*(\mathbf{x},t^*) = h_\infty^*(T^* - T_\infty^*) & \mathbf{x} \in \Gamma_3 \end{cases} \tag{3}$$

where ∇^2 represents the Laplacian operator, $T^*(\mathbf{x},t^*)$ is the sought temperature field variable, t^* denotes time ($t^* > 0$). k^* is the thermal conductivity dependent on the special variables $\mathbf{x} \in \Omega$; ρ^* is the mass density and c is the specific heat. $Q_t^* = Q_m^* + Q_r^*$ stands for the general internal heat generation per unit volume due

to metabolic heat and the laser beam. q^* represents the boundary normal heat flux defined by

$$q^* = -k^* \nabla T^* \cdot \mathbf{n} = -k^* \frac{\partial T^*}{\partial n} \tag{4}$$

n is the unit outward normal to the boundary Γ. A variable with over-bar denotes the variable being specified on given boundary. The constant T_a^* is artery temperature. The constant h_∞^* is the convection coefficient and T_∞^* is the environmental temperature. For a well-posed problem, we have $\Gamma = \Gamma_1 \cup \Gamma_2 \cup \Gamma_3$.

Finally, the initial condition is defined as

$$T^*(\mathbf{x}, t^* = 0) = T_0^*(x) \tag{5}$$

To avoid the potential numerical overflow of the present algorithm, the following dimensionless variables are employed in the analysis [16]:

$$\begin{aligned} &X = \frac{x}{L_0},\ Y = \frac{y}{L_0},\ T = \frac{(T^* - T_a^*)\,k_0}{Q_0 L_0^2},\ k = \frac{k^*}{k_0} \\ &\rho = \frac{\rho^*}{\rho_0},\ c = \frac{c^*}{c_0},\ t = \frac{t^* k_0}{L_0^2 \rho_0 c_0},\ Q_t = \frac{Q_t^*}{Q_0} \end{aligned} \tag{6}$$

where L_0 is the reference length of the biological body, k_0, ρ_0, c_0, and Q_0 are respectively reference values of the thermal conductivity, density, specific heat of tissue, and heat source term.

From Eq. (6) we derive

$$\begin{aligned} &\frac{\partial T^*}{\partial x} = \frac{Q_0 L_0^2}{k_0} \frac{1}{L_0} \frac{\partial T}{\partial X},\ \frac{\partial T^*}{\partial y} = \frac{Q_0 L_0^2}{k_0} \frac{1}{L_0} \frac{\partial T}{\partial Y} \\ &\frac{\partial^2 T^*}{\partial x^2} = \frac{Q_0 L_0^2}{k_0} \frac{1}{L_0^2} \frac{\partial^2 T}{\partial X^2},\ \frac{\partial^2 T^*}{\partial y^2} = \frac{Q_0 L_0^2}{k_0} \frac{1}{L_0^2} \frac{\partial^2 T}{\partial Y^2} \\ &\frac{\partial T^*}{\partial t^*} = \frac{Q_0 L_0^2}{k_0} \frac{k_0}{L_0^2 \rho_0 c_0} \frac{\partial T}{\partial t}, \end{aligned} \tag{7}$$

Substitution of Eq. (5) and Eq. (7) into Eq. (2) yields

$$k \nabla^2 T(\mathbf{x}, t) - \rho_b c_b \omega_b T(\mathbf{x}, t) + Q_t(\mathbf{x}) = \rho c \frac{\partial T(\mathbf{x}, t)}{\partial t} \tag{8}$$

where

$$\rho_b c_b \omega_b = \frac{\rho_b^* c_b^* \omega_b^* L_0^2}{k_0} \tag{9}$$

Correspondingly, the boundary conditions are rewritten as

$$\begin{cases} T(\mathbf{x},t) = \bar{T}(\mathbf{x},t) & \mathbf{x} \in \Gamma_1 \\ q(\mathbf{x},t) = \bar{q}(\mathbf{x},t) & \mathbf{x} \in \Gamma_2 \\ q(\mathbf{x},t) = h_\infty (T - T_\infty) & \mathbf{x} \in \Gamma_3 \end{cases} \tag{10}$$

with

$$\overline{T} = \frac{\left(\overline{T}^* - T_a^*\right) k_0}{Q_0 L_0^2},\ \overline{q} = \frac{\overline{q}^*}{Q_0 L_0},\ h_\infty = \frac{h_\infty^* L_0}{k_0},\ T_\infty = \frac{\left(T_\infty^* - T_a^*\right) k_0}{Q_0 L_0^2} \tag{11}$$

and

$$q = -k \frac{\partial T}{\partial n} \tag{12}$$

3 Transient HFS-FEM formulation

3.1 Direct time stepping

Making use of finite difference method, the derivative of temperature can be written as

$$\frac{\partial T(\mathbf{x},t)}{\partial t} = \frac{T^{n+1}(\mathbf{x}) - T^n(\mathbf{x})}{\Delta t} \tag{13}$$

where Δt is the time-step, $T^{n+1}(\mathbf{x}) = T(\mathbf{x}, t^{n+1})$ and $T^n(\mathbf{x}) = T(\mathbf{x}, t^n)$ represent the temperature at the time instances t^{n+1} and t^n, respectively.

As a result, Eq. (8) at the time instance t^{n+1} can be rewritten as

$$k\nabla^2 T^{n+1}(\mathbf{x}) - \rho_b c_b \omega_b T^{n+1}(\mathbf{x}) + Q_t(\mathbf{x}) = \rho c \frac{T^{n+1}(\mathbf{x}) - T^n(\mathbf{x})}{\Delta t} \tag{14}$$

Rearranging Eq. (14) gives

$$\nabla^2 T^{n+1}(\mathbf{x}) - \lambda^2 T^{n+1}(\mathbf{x}) = b(\mathbf{x}) \tag{15}$$

with

$$\lambda = \sqrt{\frac{\rho c}{k\Delta t} + \frac{\rho_b c_b \omega_b}{k}} \tag{16}$$

and

$$b(\mathbf{x}) = -\frac{1}{k} Q_t(\mathbf{x}) - \frac{\rho c}{k\Delta t} T^n(\mathbf{x}) \tag{17}$$

Accordingly, the boundary conditions at time instance t^{n+1} can be represented as

$$\begin{cases} T^{n+1}(\mathbf{x}) = \bar{T}(\mathbf{x}, t^{n+1}) & \mathbf{x} \in \Gamma_1 \\ q^{n+1}(\mathbf{x}) = \bar{q}(\mathbf{x}, t^{n+1}) & \mathbf{x} \in \Gamma_2 \\ q^{n+1}(\mathbf{x}) = h_\infty (T^{n+1} - T_\infty) & \mathbf{x} \in \Gamma_3 \end{cases} \tag{18}$$

The linear system consisting of the governing partial differential equation (15) and boundary conditions (18) is a standard inhomogeneous modified Helmholtz system, which will be solved by means of the present HFS-FEM and the dual reciprocity technique based on radial basis function interpolation described in the following sections.

3.2 Particular solution obtained using radial basis functions

Let T_p^{n+1} be a particular solution of the governing equation (15), we have

$$\nabla^2 T_p^{n+1}(\mathbf{x}) - \lambda^2 T_p^{n+1}(\mathbf{x}) = b(\mathbf{x}) \tag{19}$$

but does not necessarily satisfy boundary condition (18).

Subsequently, the system consisting of Eq. (15) and Eq. (18) can be reduced to a homogeneous system by introducing two new variables as follows:

$$\begin{aligned} T_h^{n+1}(\mathbf{x}) &= T^{n+1}(\mathbf{x}) - T_p^{n+1}(\mathbf{x}) \\ q_h^{n+1}(\mathbf{x}) &= q^{n+1}(\mathbf{x}) - q_p^{n+1}(\mathbf{x}) \end{aligned} \tag{20}$$

where

$$q_h^{n+1}(\mathbf{x}) = -k \frac{\partial T_h^{n+1}(\mathbf{x})}{\partial n}, \; q_p^{n+1}(\mathbf{x}) = -k \frac{\partial T_p^{n+1}(\mathbf{x})}{\partial n} \tag{21}$$

Substituting Eq. (20) into Eq. (15), we obtain the following homogeneous equation

$$\nabla^2 T_h^{n+1}(\mathbf{x}) - \lambda^2 T_h^{n+1}(\mathbf{x}) = 0 \tag{22}$$

with modified boundary conditions

$$\begin{cases} T_h^{n+1}(\mathbf{x}) = \bar{T}_h(\mathbf{x}) = \bar{T}(\mathbf{x}, t^{n+1}) - T_p^{n+1}(\mathbf{x}) & \mathbf{x} \in \Gamma_1 \\ q_h^{n+1}(\mathbf{x}) = \bar{q}_h(\mathbf{x}) = \bar{q}(\mathbf{x}, t^{n+1}) - q_p^{n+1}(\mathbf{x}) & \mathbf{x} \in \Gamma_2 \\ q_h^{n+1}(\mathbf{x}) = h_\infty \left\{ T_h^{n+1}(\mathbf{x}) - T_\infty^{n+1}(\mathbf{x}) \right\} & \mathbf{x} \in \Gamma_3 \end{cases} \tag{23}$$

where

$$T_\infty^{n+1}(\mathbf{x}) = -T_p^{n+1}(\mathbf{x}) + T_\infty + \frac{q_p^{n+1}(\mathbf{x})}{h_\infty}$$

The above homogeneous system can be solved using the hybrid finite element model described in the next section.

In what follows, we describe the solution procedure for the particular solution part $T_p^{n+1}(\mathbf{x})$. For the arbitrary right-handed source term $b(\mathbf{x})$, the particular solution $T_p^{n+1}(\mathbf{x})$ can be determined numerically by the dual reciprocity technique, in which it is essential to approximate the source term by a series of basis functions, i.e. radial basis functions (RBFs).

Let φ be a radial basis function. Then the source term $b(\mathbf{x})$ in Eq. (19) can be approximated as follows [17, 18]:

$$b(\mathbf{x}) = \sum_{j=1}^{M} \alpha_j \varphi(r_j) \tag{24}$$

where $r_j = \left\| \mathbf{x} - \mathbf{x}_j \right\|$ denotes the Euclidean distance between the field point $\mathbf{x}$ and source point $\mathbf{x}_j$, and α_j are unknown coefficients.

Making use of Eq. (24), the particular solution can be obtained as

$$T_p^{n+1}(\mathbf{x}) = \sum_{j=1}^{M} \alpha_j \Phi(r_j) \tag{25}$$

where the function is governed by

$$\nabla^2 \Phi(r_j) - \lambda^2 \Phi(r_j) = \varphi(r_j) \tag{26}$$

Taking the thin plate spline (TPS)

$$\varphi(r_j) = r_j^2 \ln(r_j) \tag{27}$$

as an example, the approximate particular solution $\Phi(r_j)$ can be obtained by the annihilator method as [19]

$$\Phi(r_j) = \begin{cases} -\frac{4}{\lambda^4} - \frac{4}{\lambda^4} \ln r_j - \frac{1}{\lambda^2} r_j^2 \ln r_j - \frac{4}{\lambda^4} K_0(\lambda r_j), & r_j \neq 0 \\ -\frac{4}{\lambda^4} + \frac{4\gamma}{\lambda^4} + \frac{4}{\lambda^4} \ln\left(\frac{\lambda}{2}\right), & r_j = 0 \end{cases} \tag{28}$$

where γ=0.5772156649015328 is Euler's constant.

3.3 Homogeneous solution using the hybrid finite element model

To perform the hybrid finite element analysis in a convenient way, the boundary conditions given in Eq. (23) are rewritten as

$$\begin{cases} T_h^{n+1}(\mathbf{x}) = \bar{T}_h(\mathbf{x}) & \mathbf{x} \in \Gamma_1 \\ \chi_h^{n+1}(\mathbf{x}) = \bar{\chi}_h(\mathbf{x}) & \mathbf{x} \in \Gamma_2 \\ \chi_h^{n+1}(\mathbf{x}) = \bar{h}_\infty \left\{ T_h^{n+1}(\mathbf{x}) - T_\infty^{n+1}(\mathbf{x}) \right\} & \mathbf{x} \in \Gamma_3 \end{cases} \tag{29}$$

with

$$\chi_h^{n+1}(\mathbf{x}) = \frac{\partial T_h^{n+1}(\mathbf{x})}{\partial n},\ \bar{\chi}_h(\mathbf{x}) = -\bar{q}_h(\mathbf{x})/k,\ \bar{h}_\infty = -\frac{h_\infty}{k} \tag{30}$$

Then, the following hybrid variational functional expressed at element level can be constructed as [18]

$$\Pi_{me} = \frac{1}{2}\int_{\Omega_e}\left(T_{,i}T_{,i} + \lambda^2 T^2\right)\mathrm{d}\Omega - \int_{\Gamma_{2e}}\bar{\chi}\tilde{T}\,\mathrm{d}\Gamma + \int_{\Gamma_e}\chi\left(\tilde{T}-T\right)\mathrm{d}\Gamma - \frac{1}{2}\int_{\Gamma_{3e}}\bar{h}_\infty\left(\tilde{T}-T_\infty\right)^2\mathrm{d}\Gamma \tag{31}$$

in which T is the temperature field defined inside the element domain Ω_e with the boundary Γ_e, $\tilde{T}$ denotes the frame field defined along the element boundary, and $\Gamma_{2e} = \Gamma_2 \cap \Gamma_e$, $\Gamma_{3e} = \Gamma_3 \cap \Gamma_e$. Note that in Eq. (31), the superscript 'n+1' and subscript 'h' are discarded for the sake of simplicity.

By invoking the divergence theorem and assuming that $\tilde{T}$ satisfies the specified temperature boundary condition (the first equation of Eq. (29)) and the compatibility condition on the interface between the element under consideration and its adjacent elements as prerequisites, variation of Eq. (31) can be written as

$$\begin{aligned}\delta\Pi_{me} = &-\int_{\Omega_e}\left(T_{,ii} - \lambda^2 T\right)\delta T\,\mathrm{d}\Omega + \int_{\Gamma_{2e}}\left(\chi-\bar{\chi}\right)\delta\tilde{T}\,\mathrm{d}\Gamma + \int_{\Gamma_e}\delta\chi\left(\tilde{T}-T\right)\mathrm{d}\Gamma \\ &+ \int_{\Gamma_{3e}}\left[\chi - \bar{h}_\infty\left(\tilde{T}-T_\infty\right)\right]\delta\tilde{T}\,\mathrm{d}\Gamma\end{aligned} \tag{32}$$

from which it can be seen that the third integral enforces the equality of T and $\tilde{T}$ along the element boundary Γ_e. The first, second and fourth integrals enforce respectively the governing equation (22), flux, and convection boundary conditions (the second and third equations in (29)).

If the internal temperature field T satisfies the homogeneous modified Helmholtz equation, i.e.

$$\nabla^2 T - \lambda^2 T = 0 \tag{33}$$

pointwise, then applying the divergence theorem again to the functional (31), we have

$$\Pi_{me} = -\frac{1}{2}\int_{\Gamma_e}\chi T\,\mathrm{d}\Gamma - \int_{\Gamma_{2e}}\bar{\chi}\tilde{T}\,\mathrm{d}\Gamma + \int_{\Gamma_e}\chi\tilde{T}\,\mathrm{d}\Gamma - \int_{\Gamma_{3e}}\frac{\bar{h}_\infty}{2}\left(\tilde{T}-T_\infty\right)^2\mathrm{d}\Gamma \tag{34}$$

which involves boundary integrals only.

In the proposed HFS-FEM, the variable T is given as a superposition of fundamental solutions $G^*(P,Q_j)$ at n_s source points to guarantee the satisfaction of Eq. (33)

$$T_h^{n+1} = \sum_{j=1}^{n_s} G^*(P,Q_j)c_{ej} = \mathbf{N}_e(P)\mathbf{c}_e,\ P \in \Omega_e, Q_j \notin \Omega_e \tag{35}$$

where c_{ej} is undetermined coefficients and n_s is the number of virtual sources Q_j applied at points outside the element.

The free-space fundamental solution of the modified Helmholtz operator can be obtained as the solution of

$$\nabla^2 G^*(P,Q_j) - \lambda^2 G^*(P,Q_j) = -\delta(P,Q_j) \tag{36}$$

and is given by [20]

$$G^*(P,Q_j) = -\frac{1}{2\pi} K_0(\lambda \left\| P - Q_j \right\|) \tag{37}$$

where $\delta(P,Q_j)$ is the Dirac delta function and K_0 denotes the modified Bessel function of the second kind with order 0.

Simultaneously, the independent frame variable on the element boundary can be defined by the standard shape function interpolation

$$\tilde{T}(P) = \sum_{i=1}^{n} \tilde{N}_i(P)d_{ei} = \tilde{\mathbf{N}}_e(P)\mathbf{d}_e,\ P \in \Gamma_e \tag{38}$$

where n is the number of nodes of the element under consideration, $\tilde{N}_i$ is the shape function and d_{ei} is nodal temperature. Their descriptions can be found in standard finite element texts and are not repeated here.

By substitution of Eq. (35) and Eq. (38) into Eq. (34) we obtain

$$\Pi_{me} = -\frac{1}{2}\mathbf{c}_e^{\mathrm{T}}\mathbf{H}_e\mathbf{c}_e - \mathbf{d}_e^{\mathrm{T}}\mathbf{g}_e + \mathbf{c}_e^{\mathrm{T}}\mathbf{G}_e\mathbf{d}_e - \frac{1}{2}\mathbf{d}_e^{\mathrm{T}}\mathbf{F}_e\mathbf{d}_e + \mathbf{d}_e^{\mathrm{T}}\mathbf{f}_e - \mathbf{a}_e \tag{39}$$

in which

$$\begin{aligned}
&\mathbf{H}_e = \int_{\Gamma_e} \mathbf{Q}_e^{\mathrm{T}}\mathbf{N}_e \mathrm{d}\Gamma,\ \mathbf{G}_e = \int_{\Gamma_e} \mathbf{Q}_e^{\mathrm{T}}\tilde{\mathbf{N}}_e \mathrm{d}\Gamma,\ \mathbf{g}_e = \int_{\Gamma_{2e}} \tilde{\mathbf{N}}_e^{\mathrm{T}}\bar{\bar{q}} \mathrm{d}\Gamma \\
&\mathbf{F}_e = \int_{\Gamma_{3e}} \bar{h}_\infty \tilde{\mathbf{N}}_e^{\mathrm{T}}\tilde{\mathbf{N}}_e \mathrm{d}\Gamma,\ \mathbf{f}_e = \int_{\Gamma_{3e}} \bar{h}_\infty T_\infty \tilde{\mathbf{N}}_e^{\mathrm{T}} \mathrm{d}\Gamma,\ \mathbf{a}_e = \int_{\Gamma_{3e}} \frac{\bar{h}_\infty T_\infty^2}{2} \mathrm{d}\Gamma
\end{aligned} \tag{40}$$

and

$$\mathbf{Q}_e = \frac{\partial \mathbf{N}_e}{\partial n} \tag{41}$$

4 Numerical results

In this section, we apply the proposed numerical model to several examples for validating and assessing its applicability and effectiveness. Values of the parameters employed in the following analysis are listed in Table 2 for convenience [21, 22].

Table 2: Control parameters related to boundary conditions

Control parameters	*Value*
Ambient temperature T_∞ (^{o}C)	0∼30
Ambient convection coefficient h_∞ (Wm^{-2}K^{-1})	40∼12500
Heat conductivity of tissue k (Wm^{-1}K^{-1})	0.2∼0.9
Laser power setting P_{in} (W)	100∼250
Absorption coefficient μ_a (m^{-1})	5∼20

4.1 Verification of the present model

To validate and assess the performance of the present HFS-FEM for analyzing the transient heat transfer of skin materials with blood perfusion and metabolic heat, a benchmark example is considered whose steady-state analytical solution is expressed as follows [6]:

$$T^*(x) = A + \frac{(T_c^* - A)\left[\mu\cosh(\mu x) + B\sinh(\mu x)\right]}{\mu\cosh(\mu L) + B\sinh(\mu L)} + \frac{B\,(T_\infty^* - A)\sinh\left[\mu\,(L-x)\right]}{\mu\cosh(\mu L) + B\sinh(\mu L)} \tag{42}$$

where

$$\begin{aligned} A &= T_a^* + \frac{Q_m^*}{\rho_b^*\omega_b^* c_b^*} \\ B &= \frac{h_\infty^*}{k^*} \\ \mu &= \sqrt{\frac{\rho_b^*\omega_b^* c_b^*}{k^*}} \end{aligned} \tag{43}$$

and L is the thickness of the skin tissue.

In the computation, the solution domain is modeled with 20 eight-node quadratic elements including 99 nodes. Three different time steps Δt =50s, 80s and 100s are employed to assess the performance of the time-stepping scheme employed in this work. It is assumed that a relative steady state is reached when the inter-iteration

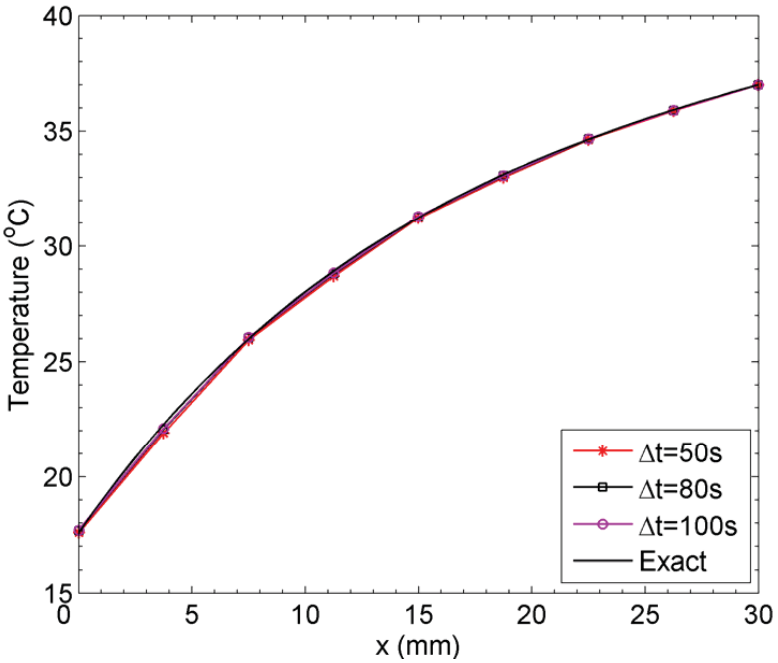

Figure 2: Steady-state temperature distribution along the x axis

difference between adjacent time instances is less than or equal to 10^{-3}. After 120, 82 and 68 iterations respectively, the corresponding distributions of temperature to these three time steps along the x axis are plotted in Figure 2. The results from the analytical solution Eq. (42) are also plotted in the figure for the purpose of comparison. As we can see from Figure 2, the numerical results from the proposed HFS-FEM are in good agreement with those of the analytical solution. At the origin point of the coordinate system, the percentage relative errors of surface temperature are respectively 0.022%, 0.45% and 0.56% for the three time steps used during the computation. The maximum value of the percentage relative errors is 1.44%, which occurs at the region close to the skin surface. Here it is necessary to point out that a smaller time step will not produce better results. It can be explained that in Eq. (16), the second term representing the blood perfusion effect $\frac{\rho_b c_b \omega_b}{k}$ is much smaller than the first term associated with time discretization $\frac{\rho c}{k\Delta t}$, that is

$$\frac{\rho c}{k\Delta t} \gg \frac{\rho_b c_b \omega_b}{k} \tag{44}$$

if the time step becomes smaller. This will cause a round-off error during the computation.

In Figure 3 the temperature distribution of skin tissues at 500s, 1000s, 3000s and steady state is displayed, from which we can see that, with the increase of time,

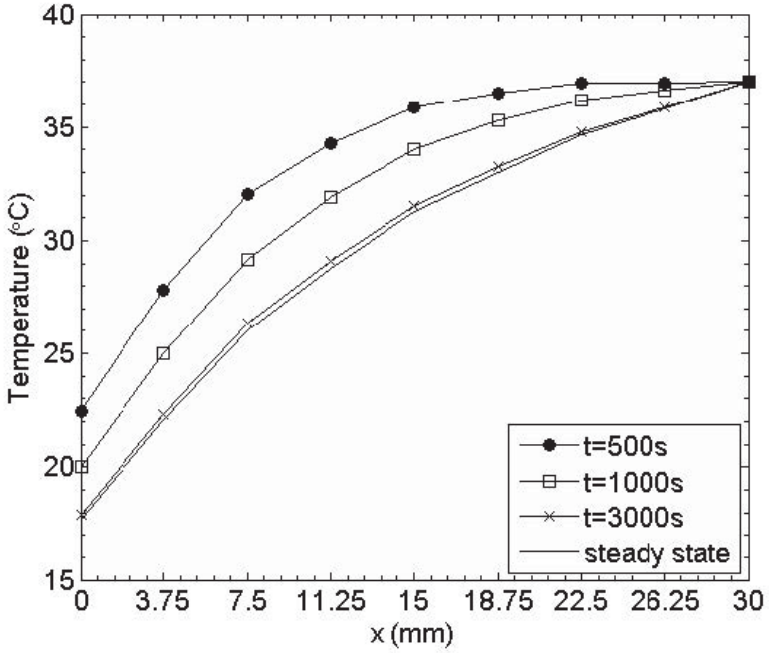

Figure 3: Temperature variation vs time along the x axis

the temperature curves do not become steeper but finally tend to a steady state. The surface temperature of the skin decreases gradually. This procedure clearly displays the propagation of the thermal wave inside the tissue and the heat exchange between the skin and the ambient fluid. Therefore, accurate results can be obtained for the transient thermal simulation in skin tissue using the present algorithm.

4.2 Sensitivity of skin temperature to different ambient fluids

The effect of environmental fluids on skin temperature is evaluated by changing the ambient convection coefficient and ambient temperature. In this study, the ambient convection coefficient is assumed to be 40, 2500 and 12500$\mathrm{Wm^{-2}K^{-1}}$, respectively, to represent different fluids such as air, oil and water [21], and the ambient temperature is set to be in the interval [0^oC, 30^oC]. The transient temperature variations are presented in Figure 4 and Figure 5 respectively. In Figure 4, the ambient temperature T_∞ is specified at 0^oC while the ambient convection coefficient changes from 40 to 12500. Figure 4 shows that there is very little difference between the numerical results for h_∞=12500$\mathrm{Wm^{-2}K^{-1}}$ and h_∞=2500$\mathrm{Wm^{-2}K^{-1}}$, whereas the difference between h_∞=40$\mathrm{Wm^{-2}K^{-1}}$ and h_∞=2500$\mathrm{Wm^{-2}K^{-1}}$is significant. The main reason for this significant difference is that the effect of forced convection increases as the convection coefficient becomes larger. The larger convection coefficient permits more heat flow from tissue to environment. As a result, the temperature at

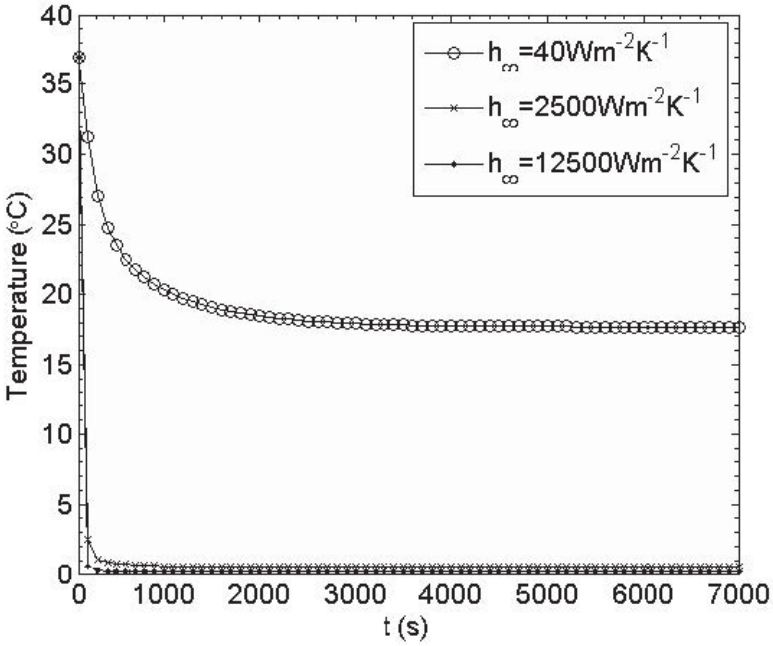

Figure 4: Surface temperature variation for various ambient convection coefficients

the convection surface is significantly reduced. Hence it is necessary to increase the convection coefficient to prevent thermal damage during treatment. However, when the convection coefficient reaches its critical value, further increase in the value of the convection coefficient cannot continuously increase the heat flow from tissue to environment. In Figure 5, the ambient convection coefficient h_∞ is set to be $40\mathrm{Wm}^{-2}\mathrm{K}^{-1}$, which corresponds to a general forced convection, while the ambient temperature changes. As expected, there is a significant increase in temperature at the origin of the coordinate system (0, 0) when the ambient temperature increases from 0^oC to 30^oC. This is because heat energy transfers rapidly from skin tissue to the environmental fluid by convection when there is a large temperature difference between the fluid and the tissue.

4.3 Sensitivity of skin temperature to tissue thermal conductivity

To study the effect of tissue thermal conductivity on skin temperature, the thermal conductivity of the tissue is assumed to vary from $0.2\mathrm{Wm}^{-1}\mathrm{K}^{-1}$ to $0.9\mathrm{Wm}^{-1}\mathrm{K}^{-1}$ in this example. In the calculation, the ambient temperature and convection coefficient are assumed to be 0^oC and $40\mathrm{Wm}^{-2}\mathrm{K}^{-1}$ respectively. The variation of the temperature along the x axis is plotted in Figure 6. As expected, the tissue temperature increases with the increase of thermal conductivity. This is reasonable, because higher values of thermal conductivity mean more heat transfer from high

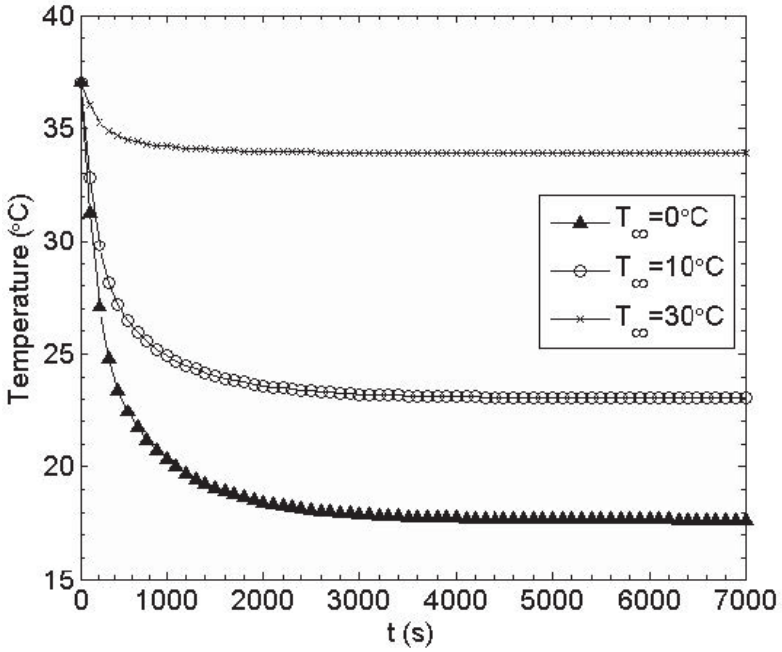

Figure 5: Surface temperature variation for various ambient temperatures

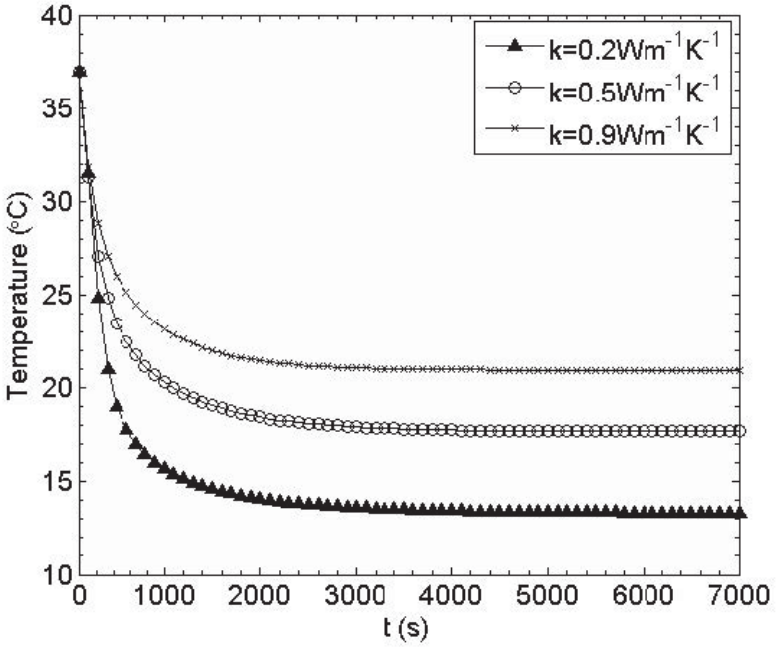

Figure 6: Surface temperature variation for various heat conductivities

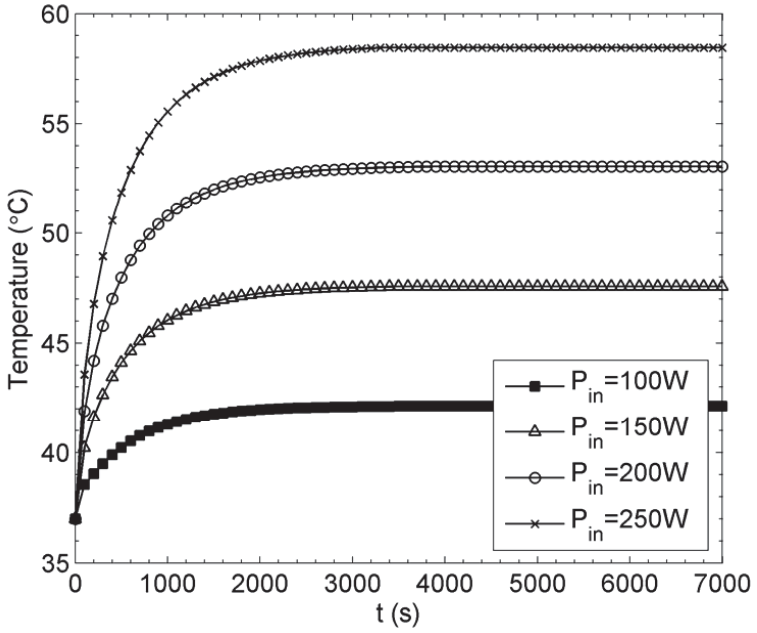

Figure 7: Temperature variation at origin for various laser power settings

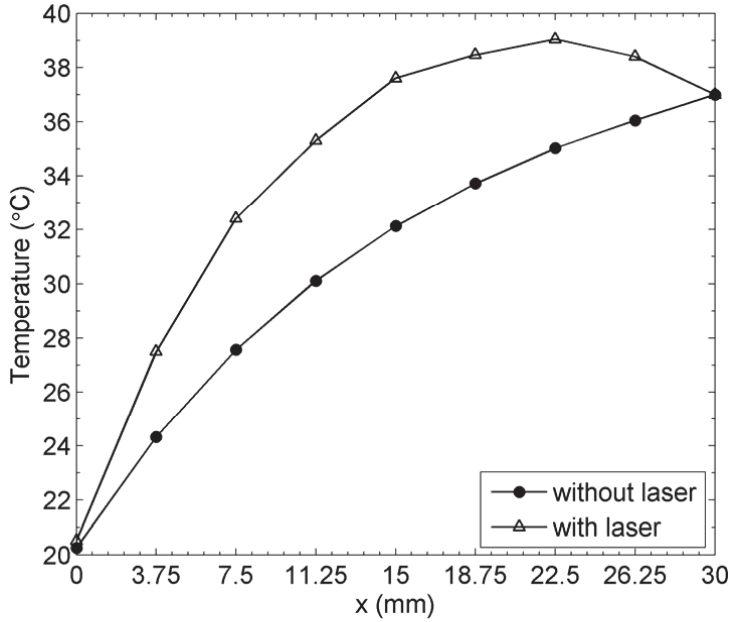

Figure 8: Steady temperature variation at origin for laser

temperature regions like the body core and arteries to the low temperature region (the skin surface), which causes the increase in surface temperature.

4.4 Sensitivity of skin temperature to different laser power settings

In the fourth example, the effect of laser heating on skin temperature is studied. In practice, there are many different types of laser for various applications. In the present work, the Beer-Lambert law is used for modeling heat absorption in two-dimensional skin tissue. The induced spatial heat source Q_r caused by the laser beam is described by Eq. (1). According to reference [15, 22], the parameters of the laser beam are taken as P_{in}=100$\sim$250W, μ_a=20m^{-1} and σ =2.85mm, respectively. The ambient temperature, ambient convection coefficient and tissue heat conductivity are respectively assumed to be 25^{o}C, 2500Wm^{-2}K^{-1}, 0.5Wm^{-1}K^{-1}. Figure 7 presents the variation of temperature at the origin (0, 0) with power settings 100W, 150W, 200W and 250W respectively. It is clearly seen from Figure 7 that the temperature significantly increases as the laser power increases, because the higher laser power generates more internal heat energy inside the tissue. In addition, it is also evident from Figure 7 that temperature will increase by the value of about 5.4 ^{o}C at the sampling point along with an increment of laser power by 50W. Figure 8 displays the steady state temperature distribution along the x axis at 4100s and it is observed that the peak value of the temperature occurs at the region close to the body core. For comparison, the temperature distribution in the absence of laser beam is also plotted in Figure 8. Finally, the spatial temperature variations in the entire tissue domain are shown in Figure 9 and Figure 10 respectively for the cases with and without laser heating. It can be clearly seen that the effect of the laser beam prevents the temperature from being one-dimensional distribution, and in the local region close to the center of the laser beam at several cutaneous penetration depths there is greater temperature gradation. Moreover, the heating effect of the laser in the thickness direction of the tissue is more obvious than that in the vertical direction.

4.5 Evaluation of skin tissue damage caused by laser

As we can see from Figure 7, the temperature of skin tissue increases rapidly along with an increase in laser power. Consequently, thermal injury or damage to biological tissue may occur, caused by laser heating. The burn degree of biological tissue is usually estimated by means of the tissue damage rate $\Omega(t)$ expressed in the following form [21, 23]:

$$\Omega(t) = \int_0^t P \exp\left(\frac{-\Delta E}{R(T+273)}\right) d\tau \tag{45}$$

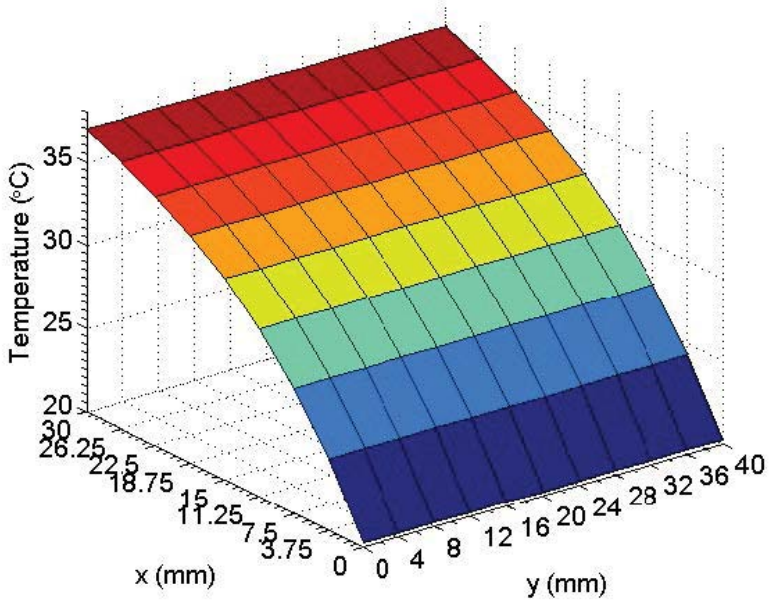

Figure 9: Steady state temperature distribution without laser

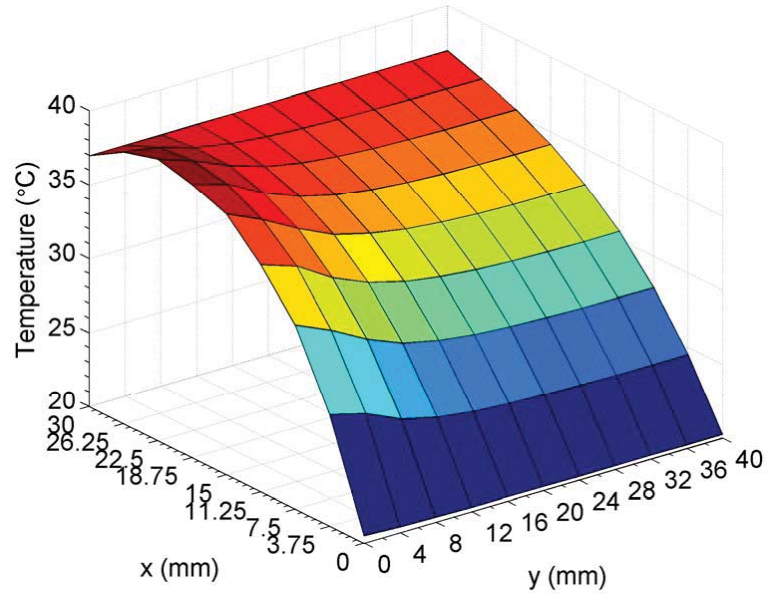

Figure 10: Steady state temperature distribution with laser

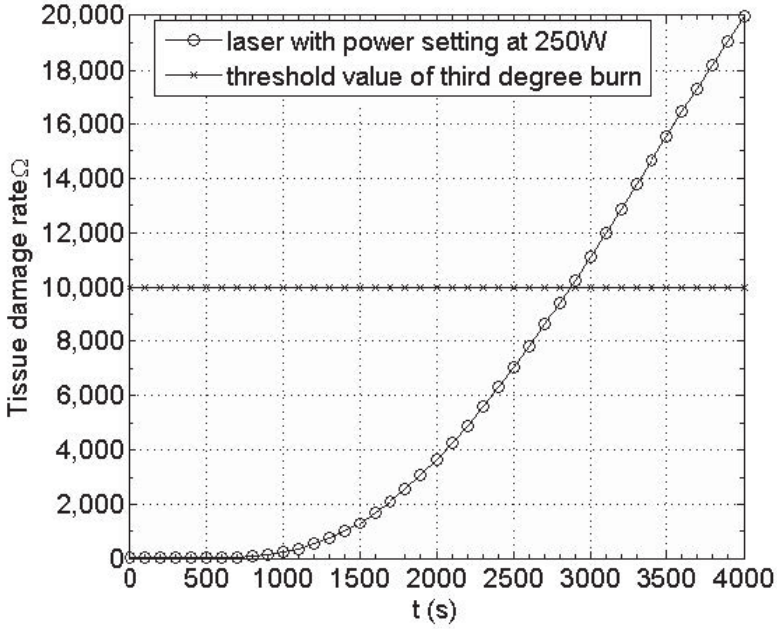

Figure 11: Skin tissue damage rate of laser with power setting at 250W

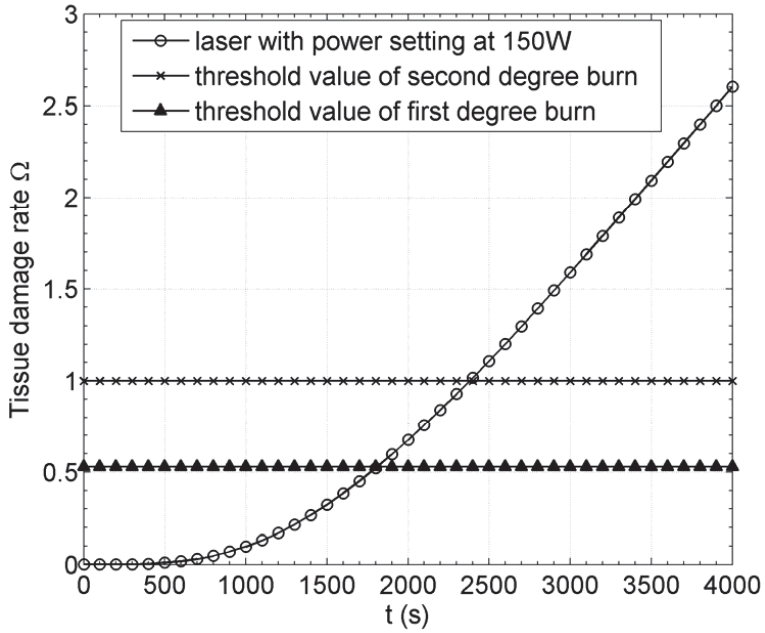

Figure 12: Skin tissue damage rate of laser with power setting at 150W 5.

where P is a constant determined by the tissue properties and local temperature. ΔE represents the activation energy and R is the universal gas constant. T is the local tissue temperature at time t. Figure 11 and Figure 12 present the numerical results for skin tissue damage rate at the point (3.75mm, 0mm) of laser heating with power setting at 250W and 150W respectively. According to the references [21, 23], the threshold values of first, second and third degree burns are Ω=0.53, Ω=1 and Ω=10^4 respectively. From Figure 11 we can see that at about 2900s the burn degree of skin tissue increases from second degree to third degree. That means that the damage to skin tissue induced by laser heating at 250W power setting becomes worse as time progresses. First and second burn degrees occur very quickly at the beginning of laser heating. Therefore, a 250W laser can cause skin damage easily and quickly. As evident in Figure 12, under 150W laser irradiation, first degree burn occurs at about 1800s and second degree burn occurs at about 2400s. It would be expected that users will avoid burning of skin tissue by reducing the laser power setting or the laser irradiation time flexibly in different applications.

5 Conclusions

In the present work, a transient HFS-FEM algorithm is developed for analyzing bioheat transfer in two-dimensional skin tissue under laser irradiation. The effects of blood perfusion, metabolic heat and spatial heating induced by a Gaussian type laser beam are considered by way of the Pennes bioheat governing equation. Numerical results from the HFS-FEM coupling with RBF are first validated by comparing with the analytical solutions, and good agreement is observed. Then, sensitivity analyses are conducted of some control parameters, namely ambient convection coefficient, ambient temperature, tissue heat conductivity and laser power setting. Finally, the burn degree of skin tissue is estimated under laser radiation with different power.

Acknowledgement: The research in this paper is partially supported by the Australian Endeavour Awards 2011 and Foundation for University Key Teacher by the Henan Province, China, under the grant no. 2011GGJS-083.

References

1. Niemz MH. Laser-Tissue Interactions-Fundamentals and Applications. 3th ed: Springer-Verlag; 2007.

2. Marqa MF, Colin P, Nevoux P, Mordon SR, Betrouni N. Focal Laser Ablation of Prostate Cancer: Numerical Simulation of Temperature and Damage Distribution. Biomed Eng Online 2011;10.

3. Shibib KS. Thermal damage due to incidental continuous CO2 laser irradiation on human skin. Therm Sci 2010;14(2): 451-58.

4. Ansari MA, Massudi R. Study of short-pulse laser propagation in biological tissue by means of the boundary element method. Lasers Med Sci 2011;26(4): 503-08.

5. Liu J, Xu LX. Boundary information based diagnostics on the thermal states of biological bodies. Int J Heat Mass Tran 2000;43(16): 2827-39.

6. Deng ZS, Liu J. Monte Carlo method to solve multidimensional bioheat transfer problem. Numer Heat Tran B 2002;42(6): 543-67.

7. Zhou JH, Chen JK, Zhang YW. Simulation of Laser-Induced Thermotherapy Using a Dual-Reciprocity Boundary Element Model With Dynamic Tissue Properties. IEEE Trans Biomed Eng 2010;57(2): 238-45.

8. Cao LL, Qin QH, Zhao N. An RBF-MFS model for analysing thermal behaviour of skin tissues. Int J Heat Mass Tran 2011;53(7-8): 1298-307.

9. Wang H, Qin QH. Hybrid FEM with Fundamental Solutions as trial functions for Heat Conduction Simulation. Acta Mechanica Solida Sinica 2009;22(5): 487-98.

10. Wang H, Qin QH. FE approach with Green's function as internal trial function for simulating bioheat transfer in the human eye. Archives of Mechanics 2010;62(6): 493-510.

11. Wang H, Qin QH. Special fiber elements for thermal analysis of fiber-reinforced composites. Engineering Computations 2011;28(8): 1079-97.

12. Wang H, Qin QH. Fundamental-solution-based finite element model for plane orthotropic elastic bodies. European Journal of Mechanics-A/Solids 2010; 29(5): 801-09.

13. Wang H, Qin QH. Fundamental-solution-based hybrid FEM for plane elasticity with special elements. Computational Mechanics 2011;48(5): 515-28.

14. Wang H, Qin QH, Kang YL. A new meshless method for steady-state heat conduction problems in anisotropic and inhomogeneous media. Archive of Applied Mechanics 2005;74(8): 563-79.

15. Frahm K, Andersen O, Arendt-Nielsen L, Morch C. Spatial temperature distribution in human hairy and glabrous skin after infrared CO2 laser radiation. BioMedical Engineering 2010;9(1): 69-86.

16. Ren Z, Liu J, Wang C, Jiang P. Boundary element method (BEM) for solving normal or inverse bio-heat transfer problem of biological bodies with complex shape. J Therm Sci 1995;4(2): 117-24.

17. Golberg MA, Chen CS, Bowman H, Power H. Some comments on the use of radial basis functions in the dual reciprocity method. Computational Mechanics 1998;21(2): 141-48.

18. Qin QH, Wang H. Matlab and C Programming for Trefftz Finite Element Methods. New York: CRC Press; 2008.

19. Muleshkov AS, Golberg MA, Chen CS. Particular solutions of Helmholtz-type operators using higher order polyhrmonic splines. Computational Mechanics 1999;23(5): 411-19.

20. Balakrishnan K, Ramachandran PA. The method of fundamental solutions for linear diffusion-reaction equations. Math Comput Model 2000;31(2-3): 221-37.

21. Ng EYK, Chua LT. Comparison of one- and two-dimensional programmes for predicting the state of skin burns. Burns 2002;28(1): 27-34.

22. Simpson CR, Kohl M, Essenpreis M, Cope M. Near-infrared optical properties of ex vivo human skin and subcutaneous tissues measured using the Monte Carlo inversion technique. Phys Med Biol 1998;43(9): 2465-78.

23. Mercer GN, Sidhu HS. A heat transfer model describing burns to the skin from automotive airbags. ANZIAM J 2005;47: 339-54.